S. Ghosh
e-mail: ghosh.5@osu.edu
Professor,
Department of Mechanical Engineering,
The Ohio State University,
Columbus, OH 43210

M. Li
Section Head,
Process Mechanics,
Alcoa Technical Center,
Alcoa Center, PA
15069

D. Gardiner
Post Doctoral Fellow,
Department of Mechanical Engineering,
The Ohio State University,
Columbus, OH 43210

A Computational and Experimental Study of Cold Rolling of Aluminum Alloys With Edge Cracking

This paper identifies various modeling issues that are necessary for successful simulation of the cold rolling process by comparing it with experiments on aluminum alloys. It combines considerable experimental studies with finite element simulations using the ABAQUS/Explicit commercial finite element code to identify and evaluate modeling parameters, such as the material properties and friction laws. Damage models are incorporated in the numerical simulations by using plasticity with damage variables e.g., the Gurson-Tvergaard model with evolving porosity and Cockcroft-Latham with damage in terms of plastic work. The 3D model predictions are compared with predictions from 2D models to understand the limitations of 2D simulations in predicting the stresses, strains and evolving damage in the rolled strip. [DOI: 10.1115/1.1645877]

1 Introduction

Cold rolling process is one of the essential elements in the manufacturing of plate, sheet, and foil products of aluminum and its alloys. Edge cracking, as shown in Fig. 1, is a commonly observed phenomenon in the cold rolling process of aluminum alloys. Subsequent edge trimming of the cracked material leads to significant productivity loss. In a typical aluminum rolling plant, only about 50% of the original material makes through to the final product form. The rest of the material is lost in various stages of the production processes and is returned to the melting pot. Edge trimming represents a large portion of this productivity loss.

The phenomenon of ductile failure in cold rolling of metals and alloys is complex. It depends on macroscopic factors such as roll geometry, rolling speed, reduction ratio or pass schedule, lubrication or friction, alloy and temper, and mechanical properties as well as on microscopic factors such as microstructure and surface micro-topography. One of the earliest models of rolling was proposed by von Karman [1] in 1925 using a Coulomb friction law for dry slipping, accounting for the interaction between the roll and the workpiece. Various analytical methods of modeling the rolling process including the 2D slab analysis have been proposed since the 1940's. Different interface friction conditions have been considered in these analyses [2]. For example, Siebel [3] proposed a constant frictional force on the interface, while Orowan and Pascoe [4] assumed sticking over the whole interface. Nadai [5] proposed a combination of dry slipping at the entry and sticking at the exit. Ford and Bland [6] considered these algorithms, along with the experimental data derived by Hill [7] to develop a method for determining approximate roll forces and torques based on the average Coulomb friction coefficient, derived from considerations of forward slip. This method showed good agreement with experimental results and is still used in industry as a relatively simple method to calculate roll forces and torques [8].

While these 2D analytical models find considerable use in industrial applications [9,10], the application of finite element method has become much more prevalent in simulating metal forming processes, because of its ability in accurately predicting the details of process variables. A large number of the finite element models that have been developed for rolling processes are essentially two dimensional, e.g., Luo's [11] investigation of different friction models and Jeswiet and Greene's [12] investigation of curvature in the rolling process. With the increase in computer processing power, the use of 3D models has recently gained popularity because of their accurate depiction of non-planar variables. Three-dimensional models have also been used for investigating surface friction parameters from considerations of the roll forces and surface pressures [13,14]. The 3D models allow the investigation of effects that cannot be considered in two dimensions, such as concave roller shapes in Lin and Lee [15], rolling strips with integral ribs in Jiang et al. [16] and slab edging in Xiong et al. [17].

The quality of products in forming processes like forging, rolling or extrusion can be adversely affected with respect to dimensional accuracy, surface finish and material integrity due to microstructural degeneration. This is triggered by particle fragmentation or de-cohesion at particle-matrix interfaces, followed by regions of plastic strain localization due to growth and coalescence of micro-cavities, and culminating into dominant cracks to advance the fracture process. In rolling experiments, Komori [18] has investigated the formation of herringbone surface defects, Gjønnes and Andersson [19] have investigated the formation of grooves and shingles and Kenmochi et al. [20] investigated the effects of micro-mechanisms on surface brightness. The effect of material ductile fracture by void nucleation, growth and coalescence phenomena, have been treated by various models, e.g., models by McClintock [21], Rice and Tracy [22], Gurson-Tvergaard models [23–25]. These models have been used in a number of metal forming failure predictions, e.g., central bursting in extrusion processes [26,27], micro-void nucleation, growth and coalescence in pipe bulging [28]. From the considerations of edge cracking, the use of a ductile damage indicator with large degree of tensile deformation has been shown to be effective in [29]. The predictive capability of these models is good with respect to stress-strain data, ductility and strain-to-failure, though in some cases the latter is over-predicted.

This paper identifies various modeling issues that are necessary for successful simulation of the cold rolling process and for understanding the role of various process parameters on the damage phenomenon. It combines experimental studies with finite element simulations using ABAQUS [30]. Since a microscopic model, involving details of the microstructural morphology and material properties, would be computationally exhaustive, a macroscopic

Contributed by the Manufacturing Engineering Division for publication in the JOURNAL OF MANUFACTURING SCIENCE AND ENGINEERING. Manuscript received October 2003. Associate Editor: S. R. Schmid.

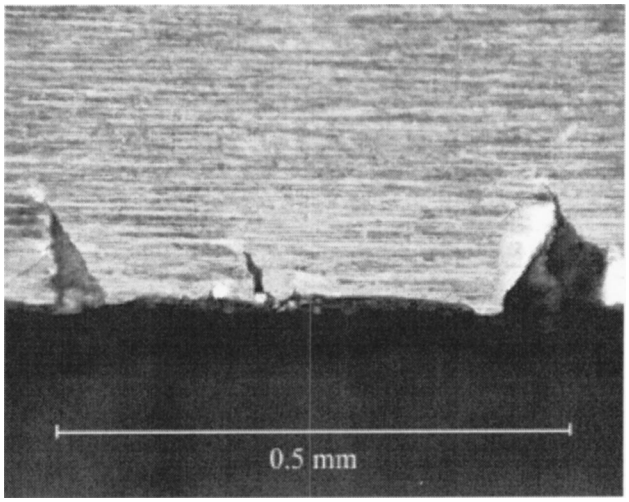

Fig. 1 Micrograph showing edge cracking occurring on the finished edge of an aluminum alloy strip during cold rolling to a reduction ratio of 80%

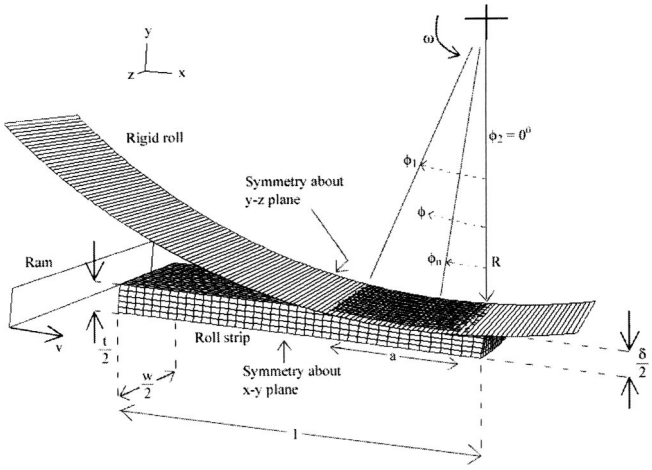

Fig. 2 A schematic diagram of the cold rolling process showing process parameters and boundary conditions

constitutive law with a microscopic variable, such as the void volume fraction, is used in this paper to understand the damage evolution process. Section 2 describes the constitutive model parameters for elastic and plastic deformation of two aluminum alloys used in the rolling experiments. The cold rolling experimental set-up and results are described in section 3 and the details the finite element simulations of the cold rolling experiments are provided in section 4. It includes assessment of friction models and damage indicators for modeling the cold rolling process. Two-dimensional analyses of the process are compared to the 3D results to examine their validity in process simulations.

2 The Material Model

The materials used for the rolling experiments are AA5049 and AA5086 aluminum alloys. The material compositions for both alloys are shown in Table 1. Finite deformation elastic-plastic constitutive relations are used for modeling the materials deformation process using ABAQUS-Explicit. The plasticity model is defined using the conventional $J2$ flow theory and isotropic hardening. Although anisotropic material response can be expected in the rolled sheets, an isotropic elasticity tensor and von Mises yield function are used for simplicity of this analysis, and also due to paucity of data in multiple directions needed for these models. The material is assumed to be strain rate independent and temperature effects are ignored, since the latter remains close to ambient in cold rolling.

The material parameters used in the cold rolling simulations are as follows. The elastic parameters for aluminum alloys are: Young's modulus=69 GPa and Poisson's ratio=0.33. The plastic parameters are determined from the true stress-true plastic strain curves, which are generated by conducting compression tests with the material coupons. These tests are conducted in the three orthogonal directions of the pre-rolled strip, viz. the rolling or longitudinal direction (x), the through-thickness direction (y) and the transverse direction (z) as shown in Fig. 2. The corresponding stress-strain curves for the AA5049 and AA5086 alloys are plotted in Fig. 3. The yield stress is 80 MPa for AA5049 and 115 MPa for AA5086. It is found that the through-thickness response is slightly different from those in the other two directions. This points to some initial anisotropy in the preformed material, on account of

Table 1 Material composition of alloying elements for AA5049 and AA5086

Alloying Element	% weight AA5049	% weight AA5086
Si	0.4	0.4
Fe	0.5	0.5
Cu	0.1	0.1
Mn	0.5–1.1	0.2–0.7
Mg	1.6–2.5	3.5–4.5
Cr	0.3	0.05–0.25
Zn	0.2	0.25
Ti	0.1	0.15
Other	0.15	0.15

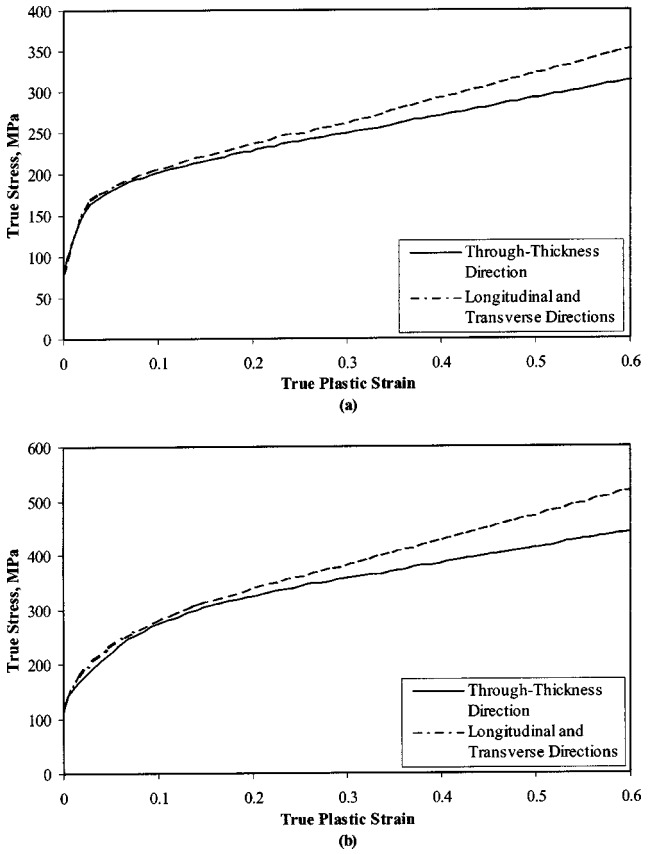

Fig. 3 Uniaxial stress-plastic strain curves obtained from compression tests of aluminum alloys (a) AA5049, (b) AA5086

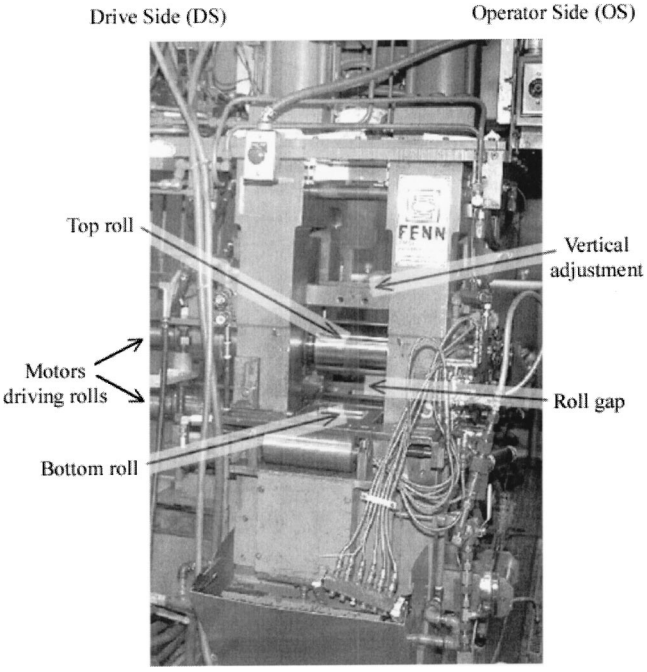

Fig. 4 A photograph of the Fenn Mill showing various mechanisms

its prior processing. However, this difference is not significant enough to warrant the introduction of an anisotropic material model in the analysis and, hence, the assumption of isotropy is considered to be justifiable in this investigation. Through the numerical simulations of the rolling processes, it is deciphered that simulations with the through-thickness material response data yield better concurrence with the experimental results. This is expected, as the direction of compression in cold rolling coincides with the through-thickness direction. Consequently, all results in this paper are with the through-thickness material response data.

3 Cold Rolling Experiments

3.1 The Experimental Set-Up. The cold rolling experiments are carried out on a FENN mill at Alcoa Technical Center, as shown in Fig. 4. The mill consists of a pair of work rolls and a pair of back-up rolls, with winding reels located at the front and the rear. The work rolls are 148.4 mm in diameter. The upper rolls are vertically adjustable, so that the roll gap can be set to any desired value. The two sides of the mill are designated DS (drive side) and OS (operator side). Two motors on the drive side power the rolls, which run at the operator-designated angular velocity. The torque supplied by the motors to the rolls is measured for each roll. Load cells are located on both sides of both rolls to measure the rolling force. Normally rolling strips are fed into the rolls by winding reels, but this requires a much longer strip than is used for experiments. Therefore, the rolling tests are hand-fed directly between the rolls, which imposes no forward or back tension loads on the strip.

3.2 Experimental Results. Four sets of single pass rolling experiments are carried out, using 43.6 mm wide strips of the AA5049 and AA5086 aluminum alloys. Three experiments use the AA5049 alloy with the mill set to reduction ratios of 20%, 35% and 50% respectively. The fourth experiment is conducted on the AA5086 alloy with a 30% reduction ratio. Various parameters for these experiments are shown in Table 2. The forces and the torques are recorded at uniform intervals of 0.025 seconds during the steady-state phase of each experiment. The values recorded for experiment 1, along with their averages, are plotted as functions

Table 2 Experimental data for the cold rolling of AA5049 and AA5086

Test	Alloy	Reduction Ratio %	Initial Thickness mm	Final Thickness mm	Average Force kN	Average Torque kN-m
1	AA5049	20	6.13	4.91	152	0.510
2	AA5049	35	6.13	3.94	221	0.969
3	AA5049	50	6.13	3.02	227	1.49
4	AA5086	30	7.72	5.46	227	1.51

of time in Fig. 5. The averaged results for all the experiments are also given in Table 2. The plots of Fig. 5 indicate that the torque measurements show relatively large fluctuations about the average value. Such fluctuations are probably due to stick slip conditions at the roll faces, as well as due to the fact that the surface conditions of the sheet are not very uniform. The material samples have direct trimmed edges from a production plant. Since the FENN mill is a very small mill, it can be highly sensitive to the surface and lubrication conditions. The relatively large difference in torsional behavior between the top and bottom rolls can be attributed to the unsymmetrical rolling conditions and the difference frictions at the top and bottom interfaces. The force measurements are nevertheless significantly more uniform in the experiments.

4 Development of the Model From Experiments

4.1 3D Geometric Model and Boundary Conditions. A three-dimensional finite element model is set up to investigate the cold rolling process, using the ABAQUS/Explicit code [30]. A quarter model is used as shown in Fig. 2 with the dimensions *l*

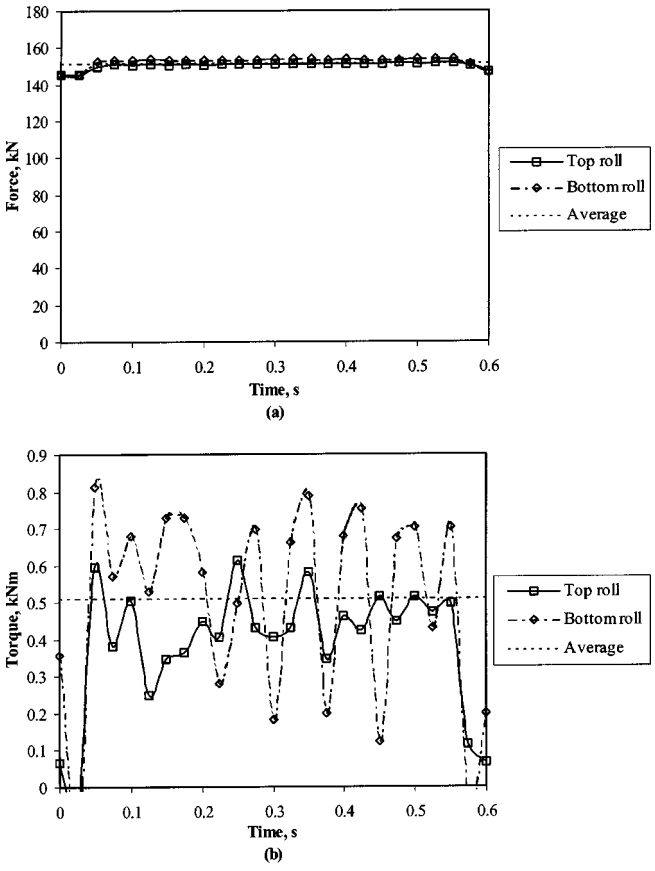

Fig. 5 (a) Force and (b) torque measurement data obtained during the steady-state part of rolling experiments with the AA5049 alloy for 20% reduction ratio

$=38.1$ mm, $w=43.6$ mm and $t=$the initial thickness, given in Table 2 for each test. The use of symmetry conditions about the two symmetry planes, viz. the x-y and x-z planes, reduces computation requirements through reduced model size. The roll gap δ, which is defined as the final thickness of the strip, is set to values given in Table 2 for the different reduction ratios. This makes an assumption of negligible elastic recovery of the roll strip on exit from the rolls. In the analysis, it is necessary to provide an initial motion to the roll strip for it to move into the roll gap. This allows the simulation to reach a steady state frictional condition between the roller and the strip, where the roll is said to bite and the strip's motion is governed by friction. This initial motion is provided through an analytical rigid frictionless surface in ABAQUS, called the ram, set to move at a constant velocity of $v=381$ mm/s. The ram speed is set to be lower than the surface speed of the roll. This allows the roll strip to separate from the ram after roll bite, so that it is subsequently dragged through the roll gap by the roll without further assistance. Steady-state results of the simulation correspond to the phase after roll bite and are not affected by the ram speed. The point where the roll strip and roll surface have identical speeds in this phase is commonly called the neutral point.

The roll is defined using a discrete rigid surface in ABAQUS, comprised of 229 4-noded 3D rigid elements (R3D4) that are equally spaced around quarter of the roll circumference, as shown in Fig. 2. It rotates with a constant angular speed $\omega=12$ rad/s about the z-axis. The roll strip is modeled as a three dimensional deformable solid with the elastic-plastic properties described in section 2. It is discretized into a mesh of 3800 8-node linear 3D brick elements (C3D8R). These elements include reduced integration with relaxed stiffness hourglass control for improved stability and convergence. Roller supports are applied on the x-y and x-z planes corresponding to symmetry planes, as shown in Fig. 2. At start, the rear of the roll strip develops an instantaneous initial velocity equal to that of the ram. A surface-to-surface contact condition is defined between the roll and the roll strip for calculating contact pressures. Relative tangential displacement is provided through a finite sliding condition, which allows large relative displacement between the surfaces. The contact-friction conditions are implemented in ABAQUS using a penalty method. The friction model used in this analysis is discussed in the next section.

4.2 The Friction Model. A number of friction models have been proposed for modeling the roll-roll strip interface conditions in the cold rolling process [2]. By far the most popular of these is the Coulomb friction model, which assumes the shear stress $\boldsymbol{\tau}$ to be proportional to the normal stress $\boldsymbol{\sigma}_\mathbf{n}$, using the friction coefficient $\boldsymbol{\mu}$ as the proportionality constant.

$$\boldsymbol{\tau}=\boldsymbol{\mu}\boldsymbol{\sigma}_\mathbf{n} \tag{1}$$

Lin and Lee [14,15] have used a Coulomb friction law in their investigations of the effect of elastic deformation of rolls. Jeswiet [31] has developed an apparatus to measure the friction in the rolling processes which produced good results in comparison to analyses based on the Coulomb friction law. A second commonly used model is the constant shear friction model, written in terms of the material yield stress $\boldsymbol{\sigma}_\mathbf{y}$

$$\boldsymbol{\tau}=\mathbf{m}\boldsymbol{\sigma}_\mathbf{y} \tag{2}$$

where $\mathbf{m}$ is a constant. Several models have combined the above two models, e.g., the Wanheim-Bay model [32].

$$\boldsymbol{\tau}=\begin{cases}\boldsymbol{\mu}\boldsymbol{\sigma}_\mathbf{n} & \forall\,\boldsymbol{\sigma}_\mathbf{n}\leqslant\dfrac{\boldsymbol{\sigma}_\mathbf{y}\mathbf{m}'}{\boldsymbol{\mu}}\\[2ex] \boldsymbol{\sigma}_\mathbf{y}\left(\mathbf{m}'+(\mathbf{m}-\mathbf{m}')\left(\mathbf{1}-\exp\left[\dfrac{\boldsymbol{\sigma}_\mathbf{y}\mathbf{m}'-\boldsymbol{\mu}\boldsymbol{\sigma}_\mathbf{n}}{\boldsymbol{\sigma}_\mathbf{y}(\mathbf{m}-\mathbf{m}')}\right]\right)\right) & \forall\,\boldsymbol{\sigma}_\mathbf{n}>\dfrac{\boldsymbol{\sigma}_\mathbf{y}\mathbf{m}'}{\boldsymbol{\mu}}\end{cases} \tag{3}$$

where $\mathbf{m}'=(1-\sqrt{1-\mathbf{m}})$. While the above models consider the shear stresses to be functions of the normal stress or yield stress, other models like the Norton model [13] have constructed the shear stresses as functions of the relative velocities between the surfaces, i.e.:

$$\boldsymbol{\tau}=-\mathbf{a}\mathbf{V}_\mathbf{r}^\mathbf{k} \tag{4}$$

where $\boldsymbol{\alpha}$ and $\mathbf{k}$ are constants and $\mathbf{V_r}$ is the relative sliding velocity. In 2D analysis of the rolling process, Luo [11] has considered using a constant shear stress model, the model by Wanheim-Bay [32], and a similar model by Stephenson [33] for modeling friction. Although this result shows little variation for the simulation conditions used, the Wanheim-Bay model was found to offer the best results. Edberg [13], considered the Wanheim-Bay and Norton friction models, but chose the Coulomb friction model for 3D analysis. The Coulomb friction model has been combined with relative sliding models in Luo [11] to improve the transition of friction stresses across the neutral point, as

$$\boldsymbol{\tau}=\boldsymbol{\mu}\boldsymbol{\sigma}_\mathbf{n}\left\{\mathbf{1}-\exp\left(-\frac{\mathbf{V_r}}{\mathbf{b}}\right)\right\} \tag{5}$$

where $\mathbf{b}$ is a constant. Various methods have been proposed for calculating the friction parameters in these models. Pavlov [34] has suggested a method of forced skidding that allows the calculation of the friction by consideration of the entry tension required on the strip to cause skidding. Whitton and Ford [35] have used a similar method with exit tension. A forward slip method for finding the mean friction coefficient has been proposed by Ford and Bland [8]. In this analysis the coefficient of friction is given as functions of $\mathbf{h}_1$ and $\mathbf{h}_2$, the thickness of strip at entry and exit respectively, $\mathbf{s}$ the forward slip and $\mathbf{R}$ the roll radius.

$$\boldsymbol{\mu}=\frac{\mathbf{h}_1-\mathbf{h}_2}{\left(\sqrt{\dfrac{\mathbf{h}_1-\mathbf{h}_2}{\mathbf{4R}}}-\sqrt{\dfrac{\mathbf{sh}_2}{\mathbf{R}}}\right)\mathbf{4R}} \tag{6}$$

The forward slip is measured on the roll strips by having two scribes on the circumference of the roll. These scribes make corresponding marks on the roll strip as it passes under the roll. The slip $\mathbf{s}$ is then given as

$$\mathbf{s}=\frac{\mathbf{l_s}-\mathbf{l_R}}{\mathbf{l_R}} \tag{7}$$

where $\mathbf{l_s}$ is the final distance between these two marks on the strip and $\mathbf{l_R}$ is the mark spacing on the roll.

4.3 Determining the Coulomb Friction Coefficient. In the present analysis rolling experiments are conducted without forward tension, and Eq. (11) is used to provide an initial estimate of the Coulomb friction coefficient in the numerical simulations. To obtain the parameter $\mathbf{s}$ in Eq. (7) from experiments, four scribes are equally spaced around the circumference of the work rolls on the Fenn mill. The final distance between the scribe marks is measured on the rolled strip using Vernier calipers. The resulting

Table 3 Calculated forward slip and average friction coefficient for the rolling experiments

Experiment	s	μ
AA5049 20%	0.040	0.33
AA5049 35%	0.040	0.19
AA5049 50%	0.041	0.17
AA5086 30%	0.037	0.22

coefficients $\boldsymbol{\mu}$ are calculated and tabulated in Table 3. The average value of the Coulomb friction coefficient $\boldsymbol{\mu}$ is 0.23 with a standard deviation of 0.07. Upper and lower limits of 0.1 and 0.4, corresponding to variation of approximately two and half times the standard deviations about the mean, are considered for providing guidance in the determination of a suitable friction model from 3D FEM simulations to be used in further process simulations.

Process simulations with reduction ratios of 20%, 35% and 50% are conducted for the AA5049 alloy to establish the friction model and parameters. Figure 6 shows the variation of the vertical roll force with the reduction ratio corresponding to different friction coefficients in the Coulomb's law. The vertical force may be calculated from the normal and tangential stresses at the roll-roll strip interface as

$$\textbf{Vertical Force} = \int_{\phi_2}^{\phi_1} (\sigma_n \cos\phi \pm \tau \sin\phi) \mathbf{R} \mathbf{w} d\phi \tag{8}$$

where the $\tau \sin\phi$ term is negative for $\phi_2 \leqslant \phi < \phi_n$ and positive for $\phi_n \leqslant \phi \leqslant \phi_1$, corresponding to ϕ_n, the angle subtended by the radial line from the neutral point to the vertical. **R** is the roll radius and **w** is the strip width. Likewise, the torque in the roll can be calculated as

$$\textbf{Torque} = \int_{\phi_2}^{\phi_1} \tau \mathbf{R}^2 \mathbf{w} d\phi \tag{9}$$

The plots in Fig. 6 clearly show that the higher values of the friction coefficient greatly over-predict the roll force at higher reduction ratios. At the lower end of the reduction ratio spectrum, the discrepancy between the model and experiments with different values of Coulomb friction, is considerably smaller. However, all the simulations under-predict the roll force at the 20% reduction ratio. This calls for an adjustment to the Coulomb friction model used in the process simulation. The experimental observation that the increase in roll separation force decreases with reduction ratio is used to guide modifications in the Coulomb friction model. An important observation, which can be made from the experimental graph in Fig. 6, is that the change in the roll force decreases markedly at higher values of the reduction ratio. For example, an increase in the reduction ratio from 20% to 35% causes a 69.8 kN increase in the roll force, while an increase from 35% to 50% only causes a 6.2 kN increase. This points to the fact that the roll force is limited by an upper bound. As shown in Eq. (12), σ_n and τ are the two stresses contributing to the roll force. The normal stress σ_n is largely affected by the bulk material elastic and plastic properties, which are predetermined by uniaxial tests and are left unchanged. Instead, an adjustment to the laws governing shear stresses at the roll-roll strip interface is viewed as an effective means of yielding desired results. Therefore, a limiting value of the shear stress at the interface is imposed on the Coulomb friction law as

$$\tau = \begin{cases} \mu\sigma_n & \forall\, \sigma_n \leqslant \sigma_0 \\ \tau_0 & \forall\, \sigma_n > \sigma_0 \end{cases} \tag{10}$$

where τ_0 is the shear stress limit and σ_0 is the normal stress where the limit is reached. Similar recommendations on the friction law have been made by Luo [11]. The corresponding roll forces using the limiting shear stress, are plotted in Fig. 7 for 20%, 35% and 50% reduction ratios. For all the three reduction ratios, the difference in the roll force values are small when calculated with μ=0.25 and μ=0.4. Therefore, a value of μ=0.25 is chosen for the Coulomb friction law in the numerical simulations, which corresponds well to the experimentally measured value of μ=0.23. Perhaps a decreasing coefficient of friction with increasing reduction ratio could yield slightly better comparison with experiments. However, this was chosen not to be included in the present paper due to lack of proper physical explanation for the sudden change as well as for simplicity. The limiting shear stress is chosen to be τ_0=82.7 MPa, since this value yields the minimum difference between the experimental and numerical results for all the three reduction ratios. Roll force and roll torque diagrams are generated, with the resulting friction model, and plotted in Fig. 8 as functions of the reduction ratio. The torque results show excellent agreement with the experiments while the force results exhibit a 20% maximum difference. The torque results, which are governed entirely by the friction force, confirm the effectiveness of the Coulomb friction rule with a limiting shear stress. The same friction model is now used to simulate a 30% reduction in the AA5086 alloy. The friction coefficient is taken to be μ=0.25, but a different τ_0 is needed for these simulations. The constant shear stress model in Eq. (6) is used to determine the value of the limiting shear stress τ_0 for the AA5086 alloy from the limiting shear stress values of the AA5049 alloy. If *m* is a constant in Eq. (2), then

$$\left(\frac{\tau_0}{\overline{\sigma}_y}\right)_{AA5049} = \left(\frac{\tau_0}{\overline{\sigma}_y}\right)_{AA5086} \tag{11}$$

where $\overline{\sigma}_y$ is the average flow stress of each alloy, defined from the true stress-plastic strain plots as

$$\overline{\sigma}_y = \frac{\int_0^{\varepsilon^p_{max}} \sigma \cdot d\varepsilon^p}{\varepsilon^p_{max}} \tag{12}$$

The average flow stresses for the two materials are found to be $\overline{\sigma}_y$=245 MPa for the AA5049 alloy and $\overline{\sigma}_y$=343 MPa for the AA5086 alloy. Using these values in Eq. (11), the limiting shear stress is calculated to be τ_0=117 MPa, for AA5086. A similar method has been used in Ford and Bland [6]. The results of the simulation with this friction model are given in Table 4. Once again, the torque exhibits an excellent match (1.3% difference) while a 27MPa error is observed for the roll force.

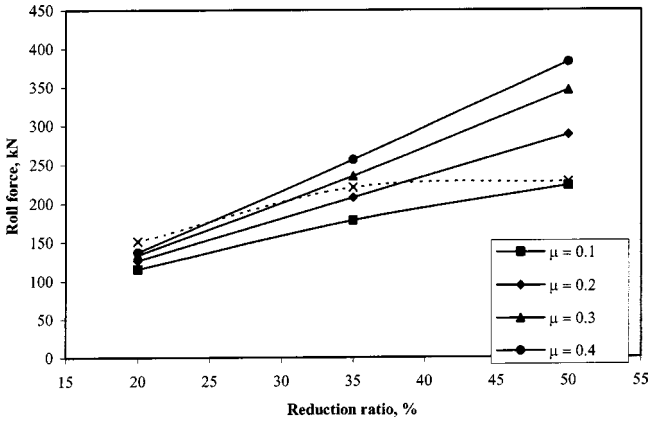

Fig. 6 Experimental and numerical values of the roll force as functions of the reduction ratio for various values of Coulomb friction coefficient

4.4 Models for Damage Evolution. As discussed in the introduction, damage evolution by void nucleation and growth plays a major role in yielding defects and ductile fracture in the workpiece. This is incorporated in the simulations of the rolling processes by the introduction of two damage models, in conjunction

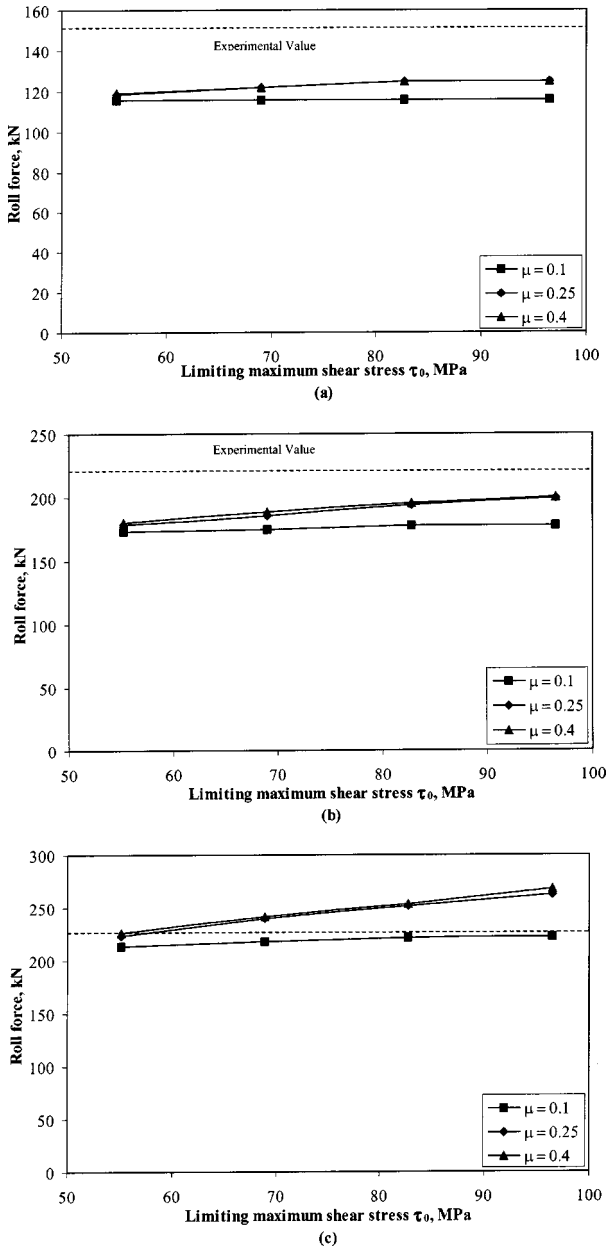

Fig. 7 Simulated values of the roll force plotted for different values of the limiting shear stress at (a) 20% reduction ratio, (b) 35% reduction ratio, (c) 50% reduction ratio

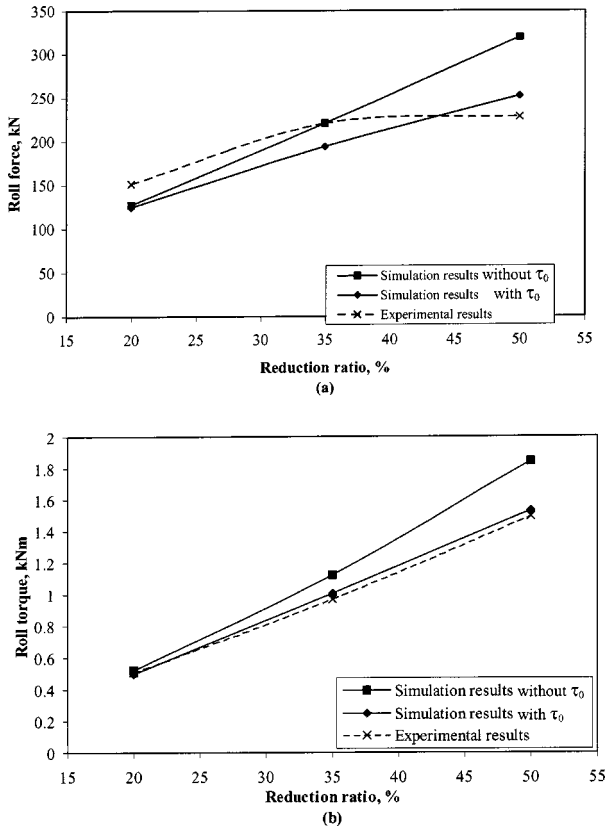

Fig. 8 Comparison of (a) roll force and (b) roll torque obtained with the friction model (σ=0.25, τ_0=82.7 MPa) with the experimental results for the AA5049 alloy

with the material laws. The first model, proposed by Gurson, Needleman and Tvergaard [23–25] is based on nucleation, growth and coalescence of voids and was developed using detailed micromechanics problem of a porous representative material element. The model introduces a yield function that is dependent on the hydrostatic pressure $\boldsymbol{\sigma}_\mathbf{p}$ and a microscopic void volume fraction $\mathbf{f}$, which is defined as the ratio of the volume of the porosities in the microstructure to the total volume of the material. The corresponding yield function is given as

$$\boldsymbol{\Phi}=\left(\frac{\overline{\boldsymbol{\sigma}}}{\boldsymbol{\sigma}_M}\right)^2+2\mathbf{q}_1\mathbf{f}\cosh\left(-\frac{3}{2}\frac{\mathbf{q}_2\boldsymbol{\sigma}_p}{\boldsymbol{\sigma}_M}\right)-(\mathbf{1}+\mathbf{q}_3\mathbf{f}^2)=\mathbf{0} \quad (13)$$

where $\overline{\boldsymbol{\sigma}}$ is the effective stress, $\boldsymbol{\sigma}_M$ is the effective microscopic tensile flow stress representing the actual microscopic stress state in the matrix and $\mathbf{q}_1$, $\mathbf{q}_2$, $\mathbf{q}_3$ are material constants. A value of $f=0$ implies a fully dense material, for which the Gurson yield criterion reduces to the Mises yield condition, while a condition that $f=1$ corresponds to a voided material with no stress carrying capacity. In general, the results in void coalescence and corresponding ductile fracture, when the void volume ratio reaches a critical value f_c. This value is assumed to be $f_c=0.3$ in this paper. The values for these constants are set to $\mathbf{q}_1=1.5$, $\mathbf{q}_2=1.0$ and $\mathbf{q}_3=2.25$, based on Tvergaard [25] and the ABAQUS Theory manual [30]. An associated flow rule is then used to evaluate the plastic strains from the yield function $\boldsymbol{\Phi}$. The rate of void evolution in this model is assumed to be due to growth of existing voids and due to nucleation of new voids and is expressed as

$$\dot{\mathbf{f}}=\dot{\mathbf{f}}_{\text{growth}}+\dot{\mathbf{f}}_{\text{nucleation}} \quad (14)$$

where $\dot{\mathbf{f}}_{\text{growth}}=(\mathbf{1}-\mathbf{f})\mathbf{D}^p_{kk}$ is the growth rate following conservation of mass, and $\dot{\mathbf{f}}_{\text{nucleation}}=\mathbf{A}\dot{\boldsymbol{\sigma}}_M$ is a strain controlled nucleation rate. The nucleation parameter A is defined in Chu and Needleman [36] as

$$A=\frac{\mathbf{f}_N}{\mathbf{S}_N\sqrt{2\boldsymbol{\pi}}}\exp\left[-\frac{1}{2}\left(\frac{\overline{\boldsymbol{\varepsilon}}^p_m-\boldsymbol{\varepsilon}_N}{\mathbf{S}_N}\right)^2\right] \quad (15)$$

where $\mathbf{f}_N$ is the volume fraction of void nucleating particles, $\boldsymbol{\varepsilon}_N$ and $\mathbf{S}_N$ are the mean and standard deviation of the nucleating strain distribution and $\overline{\boldsymbol{\varepsilon}}^p_m$ is the equivalent microscopic plastic

Table 4 Roll force and torque results for both the experiments and the 3D finite element model

Result	Roll force kN	Roll torque kN-m
Experiment	227	1.51
Simulation	254	1.53

strain. As suggested by Aravas [37], the values are chosen as $\mathbf{f}_N = 0.04$, $\boldsymbol{\varepsilon}_N = 0.3$ and $\mathbf{S}_N = 0.1$. The Gurson-Tvergaard model has been incorporated in ABAQUS, in which the time integration of the model is executed using an iterative algorithm proposed by Aravas [37].

The second damage model is based on plastic dissipation, as suggested in Cockcroft-Latham model [38] and Qyane [39]. The Cockcroft-Latham model defines a damage parameter D, for a material at a given temperature, as

$$\mathbf{D} = \int_0^{\bar{\varepsilon}_a^p} \left(\frac{\boldsymbol{\sigma}^*}{\bar{\boldsymbol{\sigma}}} \right) d\bar{\boldsymbol{\varepsilon}}^p \leqslant \int_0^{\bar{\varepsilon}_f^p} \left(\frac{\boldsymbol{\sigma}^*}{\bar{\boldsymbol{\sigma}}} \right) d\bar{\boldsymbol{\varepsilon}}^p = \mathbf{C} \tag{16}$$

where $\bar{\boldsymbol{\varepsilon}}_a^p$ is the actual equivalent plastic strain, $\bar{\boldsymbol{\varepsilon}}_f^p$ is the plastic strain at fracture, $\bar{\boldsymbol{\varepsilon}}^p$ is the equivalent plastic strain, $\bar{\boldsymbol{\sigma}}$ is the effective stress and $\boldsymbol{\sigma}^*$ is the maximum positive principal stress. This model determines the likelihood of fracture from tensile plastic deformation, by consideration of the plastic work to failure. When the damage value reaches the constant C, the material is said to have failed. While it is necessary to determine the constant C by experimentation, a general rule is that materials with very good workability will fail at a damage value between 0.8 and 1 and materials with poor workability will fail at values between 0.3 and 0.4.

5 Cold Rolling Simulations With Evolving Damage

5.1 3D Simulations. 3D simulations of cold rolling are conducted with the model described in sections 2 and 4, to understand stress, strain and damage evolution during processing. Only the 20% reduction ratio of the AA5049 alloy is considered in these simulations. No initial damage is assumed in the roll strip and the simulation is run until steady state is reached. The results in Fig. 9 show the whole strip including the leading edge. Thus the steady state values can be considered to start from a quarter of the way along the strip in the results. Figures 9(a), (b) and (c) show the contour plots of the effective residual stress after unloading, the equivalent plastic strain and the distribution of void volume fraction for the Gurson model, respectively. Figure 9(d) shows the contours of the damage parameter **D** in Eq. (16) with the Cockcroft-Latham model. It can be seen from the stress contours that the stress concentration occurs on the free edge after exiting the roll, with the maximum at the central symmetry (x-z) plane. If the individual principal directions are considered, a tensile stress is found directly under the roll in the longitudinal direction at the edge where stress concentration is later observed. This is significant because only tensile stresses cause damage through void evolution. The plastic strain on the other hand, shows a fairly uniform distribution in the unloaded portion of the rolled strip. The damage evolution predicted by the Gurson model and the Cockcroft-Latham model, as shown in Figs. 9(c) and 9(d), are consistent in that they both show considerable damage localization near the free edge and the central symmetry plane. These correspond to regions where the tensile principal stresses occur and is the place where edge cracking is found in industrial cold rolling. Since most of the remaining portion of the roll strip is subjected to compressive stresses, damage is negligible in these regions. Both damage model simulations give damage parameter values less than that needed for failure. This is consistent with the experimental observations that show no major edge cracking in AA5049 alloy until a reduction ratio of approximately 80% is reached.

5.2 Comparison of 2D Simulations With 3D Simulations. Very often, numerical simulations of materials processing are conducted in two dimensions, with assumptions of plane strain or plane stress. A major reason for this is to economize computing efforts, in addition to simplifying model developments. However, in certain situations, especially with damage, these assumptions may not be valid despite the geometric conditions of the model. Damage is typically a localized phenomenon and its distribution

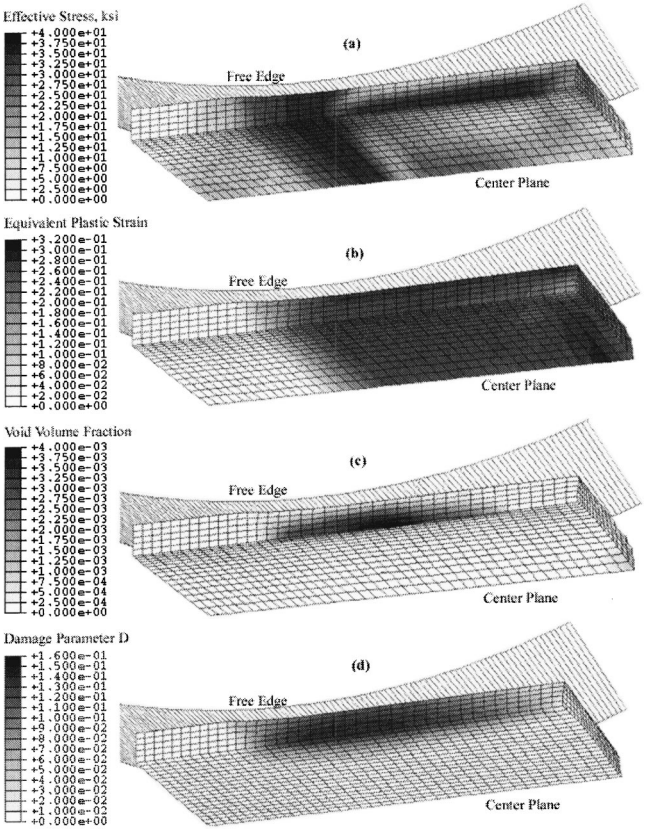

Fig. 9 Contour plots of (a) effective stress, (b) equivalent plastic strain, (c) void volume fraction in the Gurson model and (d) damage parameter in the Cockcroft Latham model, for 20% cold rolling simulations of AA5049 alloy

does not always concur with the assumptions of the plane models. 2D plane strain and plane stress simulations of the AA5049 alloy 20% reduction ratio experiments are executed in this study to determine the validity of 2D models for simulating rolling processes. The ABAQUS/Explicit code is used with the same geometric parameters as in the vertical plane of the 3D model. The same material properties and friction conditions are used. 200 bilinear quadrilateral plane strain (CPE4R) and plane stress (CPS4R) elements are used in the respective simulations.

Analytical solutions of the roll force and roll torque have been derived by Johnson [40] using the slab method for a rigid plastic material. These are given as

$$\textbf{Vertical Force} = \frac{\bar{\boldsymbol{\sigma}}_y}{2} \mathbf{a} \left[\frac{4(\boldsymbol{\lambda}+\boldsymbol{\gamma})}{\boldsymbol{\lambda}^2} (\mathbf{e}^{-\lambda X_n - 1}) + \boldsymbol{\gamma} + \frac{4\boldsymbol{\gamma}\mathbf{X_n}}{\boldsymbol{\lambda}} - 2\boldsymbol{\gamma}\mathbf{X_n^2} \right] \tag{17}$$

$$\textbf{Torque} = \frac{\bar{\boldsymbol{\sigma}}_y}{2} \mathbf{a}^2 \left[-\frac{4(\boldsymbol{\lambda}+\boldsymbol{\gamma})}{\boldsymbol{\lambda}^2} \mathbf{X_n} \mathbf{e}^{-\lambda X_n} + \frac{\boldsymbol{\gamma}}{\boldsymbol{\lambda}} \left(1 + \frac{4\mathbf{X_n}}{\boldsymbol{\lambda}} - 4\mathbf{X_n^2} \right) + \frac{2}{3}\boldsymbol{\gamma}(1+2\mathbf{X_n^3}) - \frac{2}{\boldsymbol{\lambda}} \right] \tag{18}$$

where $\mathbf{a}$ is the contact length of the roll and roll strip measured along the x-axis, x is the distance of any point along the x-axis from the exit point, $\bar{\mathbf{h}} = \mathbf{h}_1 + \mathbf{h}_2/2$, $\boldsymbol{\lambda} = 2\boldsymbol{\mu}\mathbf{a}/\bar{\mathbf{h}}$, $\boldsymbol{\gamma} = \mathbf{a}/\boldsymbol{\mu}\mathbf{R}$ and $\mathbf{X_n}$ is the neutral point given as

$$\mathbf{X_n} \equiv \frac{\mathbf{x_n}}{\mathbf{a}} \approx \frac{\bar{\mathbf{h}}}{4\boldsymbol{\mu}^2\mathbf{R}} (\mathbf{1} - \mathbf{e}^{-\boldsymbol{\mu}\mathbf{a}/\bar{\mathbf{h}}}) - \frac{1}{2} \tag{19}$$

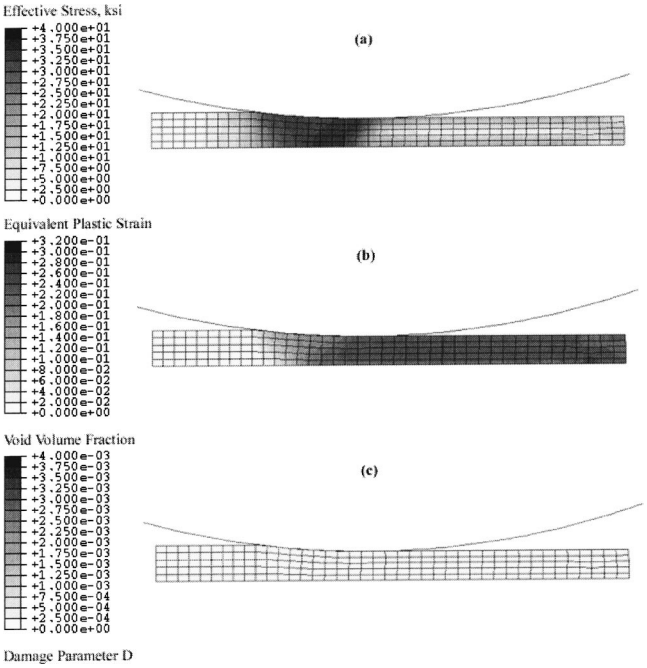

Fig. 10 Contour plots of (a) effective stress, (b) equivalent plastic strain and (c) void volume fraction for the Gurson model for plane strain simulations of AA5049 alloy to 20% reduction

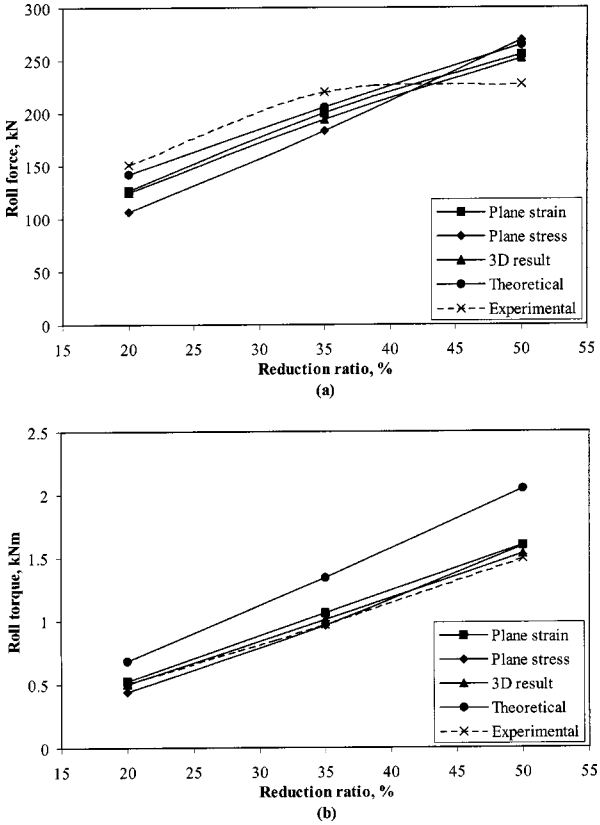

Fig. 11 Comparison of (a) roll force and (b) roll torque predictions by various 2D and 3D models

Contour plots of the effective stresses, equivalent plastic strains and void volume fraction for the plane strain and plane stress models are shown in Figs. 10 and 11. These can be compared with the 3D results given in Fig. 9. The plane strain results in Fig. 10 compare very well with the results in the central vertical section of the 3D model. However, the plane stress model does not generate satisfactory comparison with the free edge results in the 3D model. The stress concentration and the corresponding damage near the free edge are completely absent from the plane stress results. This is a consequence of the lack of tensile stresses in the plane stress simulations. Therefore, a 3D model is required to investigate edge cracking during the rolling process. Understanding edge cracking requires 3D simulation due to the uneven elongation along the trip width. The larger elongation in the rolling direction at the edge than at the center of the strip results in a tensile stress in the rolling direction at the edge and a compression stress at the center. This contributes significantly to the edge cracking.

Finally, the roll force and torque generated by the finite element simulations are compared in Fig. 11 with the experimental and analytical results. It is seen that the results for the plane strain model closely match those of the 3D simulation. The analytical solution, while reasonably accurate for the roll force, is considerably different with respect to the torque predictions. This is because the analytical solution does not include the shear stress limit, which means that the torque predicted will be higher than the model results.

6 Conclusions

In this paper, a numerical model for simulating cold rolling processes of aluminum alloys AA5049 and AA5086 is developed by comparison with experiments. The incorporation of more detailed micro-mechanics into manufacturing process simulations and design is currently under consideration. Extensive experiments on material coupon tests as well as cold rolling processes are conducted at Alcoa Technical Center. Three rolling experiments are carried out on the AA5049 alloy for reduction ratios of 20%, 35%, 50%, and one experiment on the AA5086 alloy at 30% reduction ratio. Results are recorded for the roll force and torque during steady state. The material parameters for the plasticity model, based on $J2$ flow theory with isotropic hardening, are derived from the through-thickness compression tests. A three-dimensional finite element model is set up to simulate and investigate the process using the ABAQUS/Explicit code [30]. An inverse analysis with results of simulations is conducted to determine the friction model and calibrate the friction parameters. The inverse analyses point to a Coulomb friction model with a limiting shear stress. This model produces an excellent match with the roll torque experimental results. Overall, the model seems to over-predict the roll force at larger strain or reduction ratio. This primarily attributes to the stress-train curve obtained by compression tests. At larger strains (e.g., over 30% strain), the compression tests generally give larger stresses than the real material response due to geometry effects and also due to effects inherent to the microstructure. The larger-than-reality stress at large strains was overshadowed by the friction in the torque prediction.

The 3D model is used to simulate the rolling process for the AA5049 20% reduction ratio experiment, with evolving damage. The effective stress results show a residual stress concentration at the free edge. Both the Gurson [23,24] and the Cockcroft-Latham [38] damage models show damage occurring localized at the free edge in the area that exhibits stress concentration. The predictions of the damage models concur with observations of edge-cracking in industrial process. Simulations using 2D approximations of the 3D model are also conducted. The 2D plane strain approximations predict the roll force, roll torque and strain contour results very well. The stress and damage contour results predicted by the plane strain model compare well with the central vertical plane. However, neither the plane strain nor plane stress models predict the results found at the free edge of the 3D model. The 2D approximations show no residual stress or occurrence of damage. Hence

it is concluded that the inception of damage in the cold rolling process is a three dimensional phenomenon that requires a 3D model for accurate predictions.

Acknowledgments

This work has been supported by the National Science Foundation through grant No. DMI-9912547 (Program Director: Dr. Delcie Durham), by the Ohio State University Graduate School through a Post-Doctoral Fellowship, and by Alcoa Technical Center. The authors are grateful to Dr. Simon Sheu of Alcoa Technical Center who helped perform the rolling experiments on the Fenn Mill. Computer support by the Ohio Supercomputer Center through grant # PAS813-2 is also acknowledged.

References

[1] Von Karman, T., 1925, ''On the Theory of Rolling,'' Jour. for Applied Mathematics and Mechanics (German), **5**, pp. 139–411.
[2] Ginzburg, V. B., and Ballas, R., 2000, *Flat Rolling Fundamentals*, Marcel Dekker Inc.
[3] Seibel, E., 1930, ''Resistance and Deformation and the Flow Material During Rolling,'' Stahl Eisen, **50**, p. 1769.
[4] Orowan, E., and Pascoe, K. J., 1946, ''A Simple Method of Calculating Roll Pressure and Power Consumption in Flat Hot Rolling,'' Iron and Steel Institute, **34**, pp. 124–126.
[5] Nadai, A., 1939, ''The Forces Required for Rolling Steel Strip Under Tension,'' ASME J. Appl. Mech., June, A54–62.
[6] Ford, H., and Bland, D. R., 1951, ''Cold Rolling With Strip Tension,'' Jour. of the Iron and Steel Institute, May, pp. 57–72.
[7] Hill, R., 1950, ''Relations Between Roll-Force, Torque and the Applied Tensions in Strip-Rolling,'' Proc. Inst. Mech. Eng., **163**, pp. 135–140.
[8] Kondo, S., 1975, ''An Improvement of Rolling Stability During Cold Rolling Aluminum,'' J. Lubr. Technol., January, pp. 37–43.
[9] Freshwater, I. J., 1996, ''Simplified Theory of Flat Rolling—I. The Calculation of Roll Pressure, Roll Force and Roll Torque. Inter,'' Int. J. Mech. Sci., **38**(6), pp. 633–48.
[10] Freshwater, I. J., 1996, ''Simplified Theory of Flat Rolling—II. Comparison of Calculated and Experimental Results,'' Int. J. Mech. Sci., **38**(6), pp. 649–660.
[11] Luo, C.-H., 1995, ''Modeling the Frictional Boundary Conditions in a Rolling Process,'' J. Mater. Process. Technol., **59**, pp. 373–380.
[12] Jeswiet, J., and Greene, P. G., 1998, ''Experimental Measurement of Curl in Rolling,'' J. Mater. Process. Technol., **84**, pp. 202–209.
[13] Edberg, J., 1992, *Three-Dimensional Simulation of Plate Rolling Using Different Friction Models, Numerical Methods in Industrial Forming Processes*, J. L. Chenot, R. D. Wood, O. C. Zienkiewicz, eds., Balkema, pp. 1992: 713–8.
[14] Lin, Z.-C., and Lee, S.-Y., 1997, ''An Investigation of Contact Problem Between Strip and Work Roll With a Smooth Straight Surface During Cold Rolling,'' Int. J. Mech. Sci., **39**(12), pp. 1385–1404.
[15] Lin, Z.-C., and Lee, S.-Y., 1997, ''The Effect of a Slightly Concave-Shaped Roller on Strip Shape During Rolling,'' J. Mater. Process. Technol., **70**, pp. 47–61.
[16] Jiang, Z., Xiong, S.-W., Liu, X.-H., Wang, G.-D., and Zhang, Q., 1998, ''3-D Rigid-Plastic FEM Analysis of the Rolling of a Strip With Local Residual Deformation,'' J. Mater. Process. Technol., **79**, pp. 109–112.
[17] Xiong, S.-W., Liu, X.-H., Wang, G.-D., and Zhang, Q., 1997, ''Simulation of Slab Edging by the 3-D Rigid-Plastic FEM,'' J. Mater. Process. Technol., **69**, pp. 37–44.
[18] Komori, K., 1996, ''Analysis of Herringbone Mechanisms in Sheet Rolling,'' J. Mater. Process. Technol., **60**, pp. 377–380.
[19] Gjønnes, L., and Andersson, B., 1998, ''Mechanisms of Surface Deformation During Cold Rolling of Aluminum,'' J. Mater. Sci., **33**, pp. 2469–2476.
[20] Kenmochi, K., Yarita, I., Abe, H., Fukuhara, A., Komatu, T., and Kaito, H., 1997, ''Effect of Micro-Defects on the Surface Brightness of Cold-Rolled Stainless-Steel Strip,'' J. Mater. Process. Technol., **69**, pp. 106–111.
[21] McClintock, F. A., 1968, ''A Criterion for Ductile Fracture by the Growth of Holes,'' ASME J. Appl. Mech., June, pp. 363–371.
[22] Rice, J. R., and Tracy, D. M., 1969, ''On the Ductile Enlargement of Voids in Triaxial Stress Fields,'' J. Mech. Phys. Solids, **17**(3), pp. 201–217.
[23] Gurson, A. L., 1993, ''Continuum Theory of Ductile Rupture by Void Nucleation and Growth-I, Yield Criteria and Flow Rules for Porous Ductile Media,'' J. Eng. Mater. Technol., **99**, pp. 2–15.
[24] Gurson, A. L., 1997, ''Porous Rigid-Plastic Material Containing Rigid Inclusions-Yield Function, Plastic Potential and Void Nucleation,'' *Proc. Int. Conf. Fracture, D.M.R.*, Taplin ed., Pergamon Press, **2A**, pp. 357–364.
[25] Tvergaard, V., 1981, ''Influences of Voids on Shear Band Instabilities Under Plane Strain Conditions,'' Int. J. Fract. Mech., **17**, pp. 389–407.
[26] Gelin, J. C., Oudin, J., and Ravalard, Y., 1985, ''An Improved Finite Element Method for the Analysis of Damage and Ductile in Cold Forming Processes,'' CIRP Ann., **34**(1), pp. 209–213.
[27] Aravas, N., 1986, ''The Analysis of Void Growth That Leads to Central Bursts During Extrusion,'' J. Mech. Phys. Solids, **34**(1), pp. 55–79.
[28] Oudin, J., Bennani, B., and Picart, P., 1995, ''Constitutive Models for Microvoid Nucleation, Growth and Coalescence in Elasto-Plasticity, Finite Element Reference Modeling. Materials Processing Defects,'' S. K. Ghosh and M. Predeleanu, eds., Elsevier Sci. B.V., pp. 107–123.
[29] Komori, K., 1999, ''Proposal and Use of a Void Model for the Simulation of Ductile Fracture Behavior,'' Acta Mater., **47**(10), pp. 3069–3077.
[30] ABAQUS Version 6.2. Hibbitt Karlsson and Sorensen Inc.
[31] Jesweit, J., 1998, ''A Comparison of Friction Coefficients in Cold Rolling,'' J. Mater. Process. Technol., **80**(8), pp. 239–244.
[32] Wanheim, T., and Bay, N., 1978, ''A Model for Friction in Metal Forming Processes,'' CIRP Ann., **27**, pp. 189–194.
[33] Stephenson, D. A., 1983, ''Friction in Cold Strip Rolling,'' Wear, **92**(2), pp. 293–311.
[34] Pavlov, I. M., 1938, *Theory of Rolling and Principles of Plastic Deformation of Metals* (Russian) GONTI Moscow.
[35] Whitton, P. W., and Ford, H., 1955, ''Surface Friction and Lubrication in Cold Strip Rolling,'' Proc. Inst. Mech. Eng., **169**, pp. 123–140.
[36] Chu, C. C., and Needleman, A., 1980, ''Void Nucleation Effects in Biaxially Stretched Sheets,'' J. Eng. Mater. Technol., **102**, pp. 249–256.
[37] Aravas, N., 1987, ''On the Numerical Integration of a Class of Pressure-Dependent Plasticity Models,'' Int. J. Numer. Methods Eng., **24**, pp. 1395–1416.
[38] Cockcroft, M. G., and Latham, D. J., 1968, ''Ductility and the Workability of Metals,'' J. Inst. Met. , **96**, pp. 33–39.
[39] Oyane, M., 1972, ''Criteria of Ductile Fracture Strain,'' Jour. of the Society of Mechanical Engineers, **15**(90), pp. 1507–1513.
[40] Johnson, K. L., 1985, *Contact Mechanics*, Cambridge University Press.